nature communications

Article

https://doi.org/10.1038/s41467-024-53025-7

Agile manipulation of the time-frequency distribution of high-speed electromagnetic waves

Received: 11 November 2023

Accepted: 24 September 2024

Xinyi Zhu, Benjamin Crockett, Connor M. L. Rowe, Hao Sun & José Azaña

Controlling the temporal evolution of an electromagnetic (EM) wave's frequency components, the so-called time-frequency (TF) distribution, in a versatile and real-time fashion remains very challenging, especially at the high speeds (> GHz regime) required in contemporary communication, imaging, and sensing applications. We propose a general framework for manipulating the TF properties of high-speed EM waves. Specifically, the TF distribution is continuously mapped along the time domain through phase-only processing, enabling its user-defined manipulation via widely-available temporal modulation techniques. The time-mapping operations can then be inverted to reconstruct the TF-processed signal. Using off-the-shelf telecommunication components, we demonstrate arbitrary control of the TF distribution of EM waves over a full bandwidth approaching 100 GHz with nanosecond-scale programmability and MHz-level frequency resolution. We further demonstrate applications for mitigating rapidly changing frequency interference terms and the direct synthesis of fast waveforms with customized TF distributions. The reported method represents a significant advancement in TF processing of EM waves and it fulfills the stringent requirements for many modern and emerging applications.

User-defined manipulation of the temporal properties of electromagnetic (EM) waves is key to many important applications in such diverse fields as telecommunications, sensing, metrology, biomedical imaging, and quantum processing[1–3]. Within these fields, the regime of EM waves from the microwave (radio frequency, RF) to the optical domain is of particular interest because these waves enable information encoding and manipulation at high speeds. The most straightforward approach to manipulate the temporal properties of such waves is through "temporal modulation" methods[4–8]. On the other hand, a temporal wave is often described using its frequency-domain (or Fourier transform) representation, which describes the relative complex weights between the frequency components of a wave[9]. Many important tasks (multiplexing, impairment mitigation etc[2,10–12].) require the wave to be manipulated along this domain through linear "frequency filtering" rather than along its temporal representation[1,13,14]. However, in practice, the frequency spectrum of an incoming signal is rarely stationary but changes over time. As a result, the most general manipulation of a wave requires processing its joint time-frequency (TF) distribution, which describes the temporal evolution of the wave frequency content.

A widely used TF representation is the short-time Fourier transform (STFT), also known as the spectrogram, which is obtained by windowing (or truncating) consecutive short temporal segments of the wave of interest and Fourier transforming each one of these segments[15]. As illustrated in Fig. 1a–c, a target manipulation of the joint TF distribution of a given wave cannot be generally achieved by temporal modulation or frequency filtering. Considering that most waves encountered in practice are nonstationary, there is a fundamental interest in finding ways to manipulate their joint TF distribution. Moreover, this capability is becoming increasingly important to

Institut National de la Recherche Scientifique - Centre Énergie Matériaux Télécommunication (INRS-EMT), 800 de la Gauchetière Ouest, Suite 6900, Montréal, QC, Canada. e-mail: jose.azana@inrs.ca

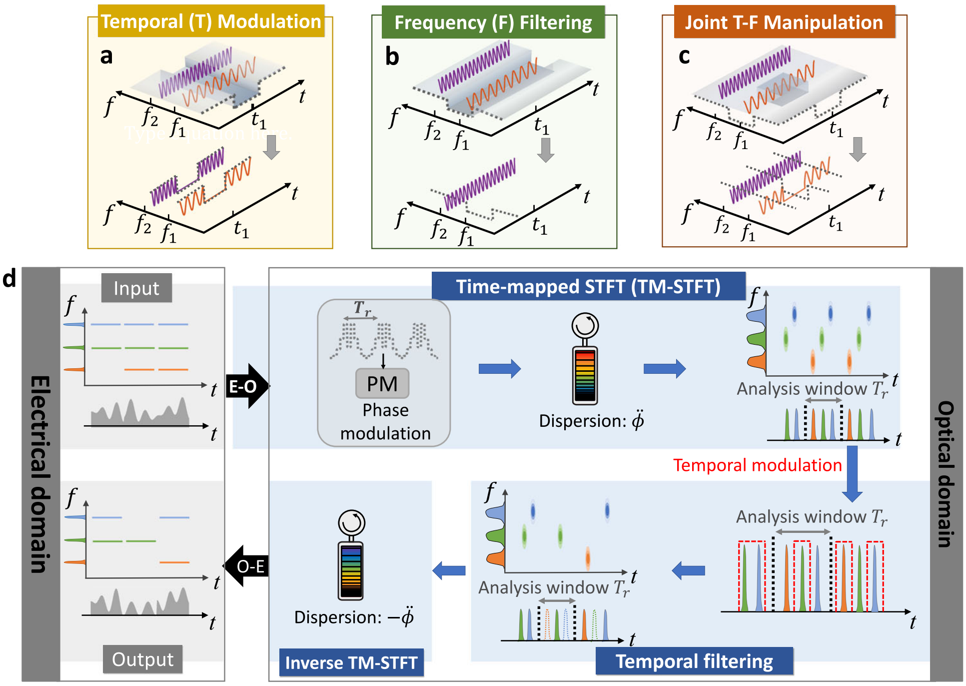

Fig. 1 | Joint time-frequency filtering concept. a–c We target to eliminate a single frequency tone around a prescribed time t_1 of an electromagnetic (EM) wave, which is composed of two different single-frequency components (f_1 and f_2, respectively). This operation cannot be implemented using temporal modulation (**a**) or frequency filtering (**b**). **c** We show how the target manipulation requires modulating (or filtering) the joint time-frequency (TF) energy distribution of the wave. **d** Principle of the proposed concept for user-defined joint TF filtering of an EM wave. An input nonstationary microwave signal consists of three different frequency components. We consider that only two components are present in the first temporal segment of the signal to illustrate the case of an input non-stationary waveform. We show here how the proposed TF filtering scheme can be designed to preserve/eliminate a prescribed set of frequency components in different signal temporal segments. For this purpose, the input microwave signal is first modulated on an optical carrier (electro-optic, E-O, conversion). The optical wave then undergoes two suitable phase transformations, implemented through temporal phase modulation with a discretized quadratic phase pattern followed by a quadratic spectral phase filtering with a group-velocity dispersive medium (e.g., a reflective chirped fibre Bragg grating). These phase transformations induce a continuous mapping of the time-varying frequency spectrum of the signal, or its two-dimensional (2D) joint TF distribution, along the time domain. This distribution can then be easily manipulated at will using temporal modulation techniques (temporal filtering pattern indicated by the red-dashed traces). For the considered microwave photonics filtering scheme, recovering the processed wave simply involves compensating the input group-velocity dispersion and a photodetection step to transfer the optical processed wave back into the electrical domain. E-O: Electrical to Optical conversion, O-E: Optical to Electrical conversion, PM: electro-optic Phase Modulator.

achieve the desired advanced functionalities and overall performance in many modern and emerging applications, including next-generation telecommunication systems[16,17] and intelligent remote sensing platforms (Radar and Lidar)[3,18,19]. For instance, to improve the spectral efficiency of modern communication systems, cognitive radio and optical schemes are increasingly being employed[20,21], requiring software-defined architectures that enable dynamic spectrum allocation and control. Sophisticated coding strategies are also needed where the desired information is encoded along the joint TF variations of the wave in a rapidly adaptable manner, such as in the case of ultrafast frequency-hoping systems[22]. Radar systems often operate in dynamic and challenging environments where reconfigurable manipulation of the frequency spectrum of the captured waves is highly desired to enhance performance, versatility, and adaptability[3,23]. In these applications, the required wave processing operations may include selecting or deselecting a set of frequency bands[24], filtering out some undesired interference or noise-like components from the incoming wave[25], or other more sophisticated manipulations on the complex wave spectrum[26]. The key feature is that these dedicated filtering operations in the aforementioned applications need to be reconfigured at a very high speed, in a nanosecond scale or even faster[26,27], while offering a set of specifications commensurate with the target performance, including operation over broad frequency bandwidths, e.g., over tens of GHz[28]. In addition, in these practical applications where a timely and accurate response is critical, processing must be performed with exceptionally low latency. In such contexts, high latency can have significant and potentially detrimental consequences[29]. For instance, real-time analysis and processing are essential in radar systems to ensure operational effectiveness and safety, as delays can impact response times and tracking accuracy. Similarly, next-generation networks face increasing demands for low-latency processing due to rising data rates and a growing number of users. It is generally accepted that in the 6G communication framework, these applications would require latencies in the sub-ms or even µs range[30].

The realisation of this wave processing paradigm requires the implementation of a dynamic or time-varying filtering (TVF) process, in contrast to the (quasi-)static time-invariant filtering that is implemented by conventional frequency filters, as illustrated in Fig. 1a–c. Furthermore, towards a full manipulation of the wave joint TF distribution, one should be able to programme and reconfigure the filter's spectral response in a user-defined, arbitrary manner and at a speed as fast as the frequency resolution offered by the filter[15], see "Methods". Arbitrary joint TF filtering can be readily implemented using digital signal processing (DSP). However, this requires detection and digitisation of the complex-field wave profile followed by conversion of the processed digital profile back into an analogue wave. Moreover, for real-time wave manipulation, this procedure is very challenging when the wave variations are faster than just a few hundred MHz. This requires processing the acquired signal with a rate of about a few million FTs per second and a corresponding time resolution in the microsecond range, specifications that are within the operation limits of present real-time DSP engines[31]. Alternatively, radio frequency (RF) filters[32,33] have been demonstrated to enable discrete tuning of some of the filter's spectral response features (e.g., centre frequency and bandwidth), though over a limited operation bandwidth, up to a few GHz. Optical filtering offers much broader operation bandwidths, and technologies are available that allow for versatile reconfigurability of the filter's spectral response[1,34]. However, the reconfigurability speed of these schemes (typically in the kHz range) remains orders of magnitude slower than the frequency resolution they can offer (typically in the GHz range), thus being unsuited for general TF signal manipulation tasks. Photonic processing has also been used for filtering high-speed microwave signals, so-called microwave photonic filters (MPFs)[14]. Some of these technologies offer an important degree of reconfigurability though still largely insufficient to enable a full arbitrary control of the wave joint TF distribution, either because of their intrinsically slow reconfiguration speed[35–37], because fast tuning is restricted to some of the filter's main specifications only (e.g., central frequency, or phase shift)[25,38–41], and/or because they are limited to implementing a very specific TF filtering operation[42].

In this work, we propose a concept for user-defined real-time manipulation of the joint TF distribution of EM waves directly in the analogue domain, ideally suited for operation on high-speed waves. Using this concept, we conceive and demonstrate a photonics scheme for TF processing of microwave and optical signals. The proposed approach combines the versatility of the DSP approach with the performance (e.g., processing speed and bandwidth) of a photonic solution. As illustrated in Fig. 1d, our strategy involves mapping the TF distribution (the STFT) of the incoming wave along the time domain in a continuous and gapless manner[41,43–46], which in turn enables a user-defined manipulation of the wave's TF distribution through the many available temporal modulation techniques. Since the time-mapped STFT is achieved using two consecutive phase transformations (along the temporal and spectral domains, respectively), the processed wave can be recovered by simply applying the opposite phase manipulations. This platform allows us to achieve an arbitrary manipulation of the joint TF distribution of the input microwave signal over a full bandwidth up to 92 GHz, with rapid tuning speeds in the nanosecond range and with a fine frequency resolution, down to a few hundreds of MHz. Through the implementation of the temporal filtering step using electro-optic modulation, the unit can be programmed electronically to provide any desired dynamic spectral response, with a reconfigurability speed inherently determined by the filter's frequency resolution, as needed for full manipulation of the wave TF distribution. We demonstrate the use of this concept for the realisation of important functionalities beyond the potential of present technologies, including the mitigation of nonstationary interference terms in broadband signals and the direct synthesis of high-speed waves with user-defined sophisticated TF distributions.

Results

Operation principle

The STFT or spectrogram (squared magnitude of the STFT) of a given input signal provides the Fourier transform, or frequency spectrum, of consecutively truncated short segments of this input signal[15], effectively providing a faithful representation of the signal's joint TF representation. Figure 1d shows a schematic of a specific implementation of the proposed concept for real-time joint TF filtering aimed at processing microwave signals using a photonic platform. The microwave signal under test (SUT) is first upconverted to the optical domain, and the STFT of the optical wave is then continuously mapped along the time domain using a configuration referred to as a Talbot array illuminator (TAI) spectrogram[46] (see "Methods"). In particular, this method enables capturing changes in the signal frequency spectrum every prescribed analysis period T_r, in such a way that each of the analysed spectra is time mapped along adjacent time slots, each with a duration T_r. As expected for an STFT analysis, each truncated signal spectrum exhibits a frequency resolution (minimum spacing between two frequency components that are resolved by the Fourier representation) of the order of the inverse of T_r[46]. Once the STFT is mapped along the time domain, the two-dimensional (2D) joint TF distribution of the SUT can be modified at will using temporal modulation methods. Specifically, the frequency spectrum information of the SUT can be modified in amplitude and/or in phase, every analysis period T_r. Moreover, each spectrum can be manipulated with a resolution that is ultimately limited by the frequency resolution of the performed spectrogram. Notice that this requires the temporal filtering function to be sufficiently fast, of the order of the analysis bandwidth B of the implemented STFT analysis (see "Methods").

To recover the processed waveform, one just needs to invert the time and frequency-domain phase transformations used for the calculation of the STFT. This means propagating the processed waveform through a dispersive medium providing the exact opposite spectral phase response of the first one (i.e., opposite dispersion$-\ddot{\phi}$), followed by a similar temporal phase modulation compensation process. Since our scheme is aimed at TF processing of amplitude encoded optical signals (upconverted microwave signals), the latest phase modulation compensation is not necessary, see Fig. 1d. Indeed, the processed microwave signal is down-converted to the microwave domain by photodetection, irrespective of the residual optical phase.

Experimental demonstrations

In the first experiment, we target filtering in (i.e., selecting) a single linear chirp component from a double-chirped microwave signal, e.g., emulating an electronic signal received from an antenna, as shown in Fig. 2 (see a more detailed schematic in Supplementary Fig. 6). Specifically, the SUT shown in Fig. 2a, b is composed of two superimposed linearly-chirped sinusoidal waveforms labelled S_1 and S_2, respectively, extending over a frequency range of ~46 GHz (full optical bandwidth of ~92 GHz). The SUT is programmed with non-uniform amplitude to pre-compensate for the bandwidth limitation/roll-offs of both the electro-optic March-Zehnder Modulator (MZM) and the RF amplifier. This ensures a nearly flat amplitude of the incoming optical signal that undergoes processing (see Supplementary Fig. 2). Notice that only the positive frequency axis is represented in the 2D spectrogram plots shown throughout this communication for clarity. The microwave SUT is then modulated on a continuous-wave (CW) laser source. The modulated optical signal is then analysed by the TAI spectrogram, providing access to the full (double sideband) frequency spectrum of the input SUT along the time domain, with a full analysis bandwidth of 92 GHz, every slot of duration $T_r = 1.5$ ns, and with a corresponding frequency resolution $\delta\omega \sim 2\pi \times 660$ MHz, i.e., allowing for about 139 analysis points per spectrum. Figure 2c shows the measured time-mapped spectrogram (TM-SP) of the SUT with zoomed-in regions over different analysis periods (each with a duration of T_r). Note that we highlight the positive side of the spectrum for each zoomed-in waveform, and the equivalent frequency axis is marked at the top of each plot. As expected, the TM-SP shows the two different frequency components of the SUT (i.e., S_1 and S_2) along each analysis window. The 2D representation in Fig. 2d was obtained from the output temporal trace by vertically plotting adjacent analysis windows (see "Methods").

The time-mapped STFT is then processed by the user-defined time-varying filter with a frequency resolution of 660 MHz. This requires the implementation of a time-domain filtering mask with a time width of ~10.8 ps, commensurate with available components, see "Methods". Specifically, the filtering mask is imposed on the time-mapped STFT through an electro-optic Mach-Zehnder modulator (MZM) driven by an electronic arbitrary waveform generator (AWG). In this example, the temporal filtering pattern, shown in Fig. 2e, is

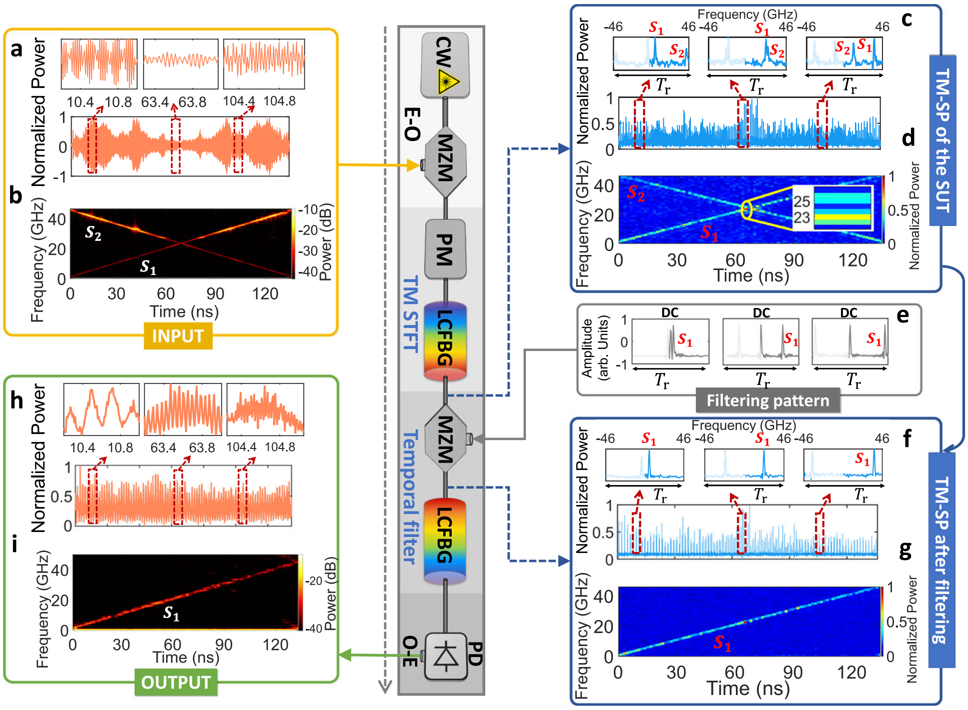

Fig. 2 | Demonstration of broadband joint time-frequency (TF) filtering with nanosecond resolution. The experimental setup is shown at the centre of the figure. **a** Temporal trace of the SUT, involving two linearly-chirped sinusoidal waveforms (‘S_1’ and ‘S_2’) and the zoomed-in traces corresponding to three different sections of the SUT. **b** Numerical spectrogram of the generated SUT with pre-compensation, depicting the temporal evolution of the frequency spectrum and the uneven intensity. **c** Measured TM-SP with several zooms around three different relevant time analysis periods. We note that the TM-SP function exhibits a significant component at the centre location of each analysis window, corresponding to the optical carrier frequency; however, this term is strongly attenuated in the representation of the TM-SP traces shown here to facilitate observation and interpretation of the obtained TF distributions of the analysed optical signals. **d** 2D representation of the signal joint TF distribution that is numerically rescaled from the output measured temporal trace of (**c**) showing a close-up of the obtained distribution near the cross point of the two chirped signals. **e** Three zooms of the temporal filtering pattern with each pulse width of $\sim t_s$, reconfigured every $T_r = 1.5$ ns. The varying time location of the filtering mask along each time slot aligns with the corresponding frequency terms of the increasing frequency-chirp component (S_1) in order to filter in this component from the SUT. **f** The measured output after temporal modulation with the designed filtering pattern shows that the temporal pulses representing the frequency components of S_2 are strongly attenuated. **g** The 2D representation of the TM-SP that is obtained after the temporal modulation. **h** Temporal trace of the processed microwave signal recovered after dispersion compensation and photo-detection, with the same zoomed-in regions as the input in (**a**). **i** Numerical spectrogram of the processed measured signal, confirming that S_2 is nearly suppressed and a pure linear chirp with increasing frequency (S_1) is recovered. SUT: Signal Under Test, TM-SP: Time-Mapped Spectrogram, STFT: Short-time Fourier Transform, 2D: two-dimensional, CW: Continuous-Wave laser, MZM: electro-optic Mach-Zehnder Modulator, PM: electro-optic Phase Modulator, LCFBG: Linearly Chirped Fibre Bragg Grating, PD: Photo-Diode.

designed to select (i) the two temporal pulses corresponding to the target chirped waveform (i.e., negative and positive frequency components of S_1) from the four frequency components of the two crossing chirps and (ii) a central pulse to select the optical carrier (see “Methods”). The filtering pattern is then reconfigured every T_r, i.e., at a tuning speed of $1/T_r \sim 660$ MHz, of the order of the frequency resolution of the performed filtering operation. Figure 2f shows the measured temporal waveform at the output of the MZM used for TF filtering. The pulses representing the frequency components of S_2 are strongly reduced with respect to the S_1 components, as shown in the representation of the resulting TM-SP in Fig. 2g. Finally, the microwave TF-filtered waveform is recovered, and the measured processed microwave signal is shown in Fig. 2h. The corresponding numerical spectrogram is also shown in Fig. 2, confirming a strong reduction of the unwanted decreasing chirp component.

To provide further evidence on the reconfigurability of the spectral response that is provided by the demonstrated time-varying filtering scheme, in terms of the passband shape, bandwidth, and tuning frequency, we have performed a standard characterisation of the RF spectral response of the microwave photonics filtering scheme in Fig. 2. This characterisation has been carried out under different temporal filtering specifications, i.e., by programming the corresponding modulation pattern, and the obtained results are presented in the Supplementary Fig. 5.

In dynamic practical environments, involving 5G and automotive radar systems[29,47,48], interference or jamming can significantly impact detection or sensing performance. In automotive radar systems, mutual interference from other radars can degrade sensitivity and detection capabilities, potentially leading to hazardous situations[47]. These radar systems typically operate in the millimetre-wave range (with potential instantaneous bandwidth exceeding 30 GHz)[49] and necessitate real-time mitigation of interferences and noise. In our subsequent results, we demonstrate the implementation of our proposal for user-defined interference mitigation over tens-of-GHz of instantaneous bandwidth through a suitable design of the time-frequency filtering response.

We use an input SUT consisting of a set of frequency-changing interferences along a broadband double-chirped signal. This spectrogram scheme is redesigned to offer a narrower frequency resolution (i.e., 110 MHz) while maintaining the full analysis bandwidth to $1/t_s \sim 92$ GHz, corresponding to ~ 836 analysis points per spectrum. We achieved this by increasing the phase modulation period (time resolution of the implemented spectrogram) to $T_r \sim 9$ ns (see “Methods”), as shown in Fig. 3. This scheme is then used to remove the undesired interferences from the SUT. This requires the design of a multi-passband filtering mask consisting of four square-like pulses along every analysis period (two pulses for each of the chirped components to be filtered in) in which the inter-pulse spacing is changed

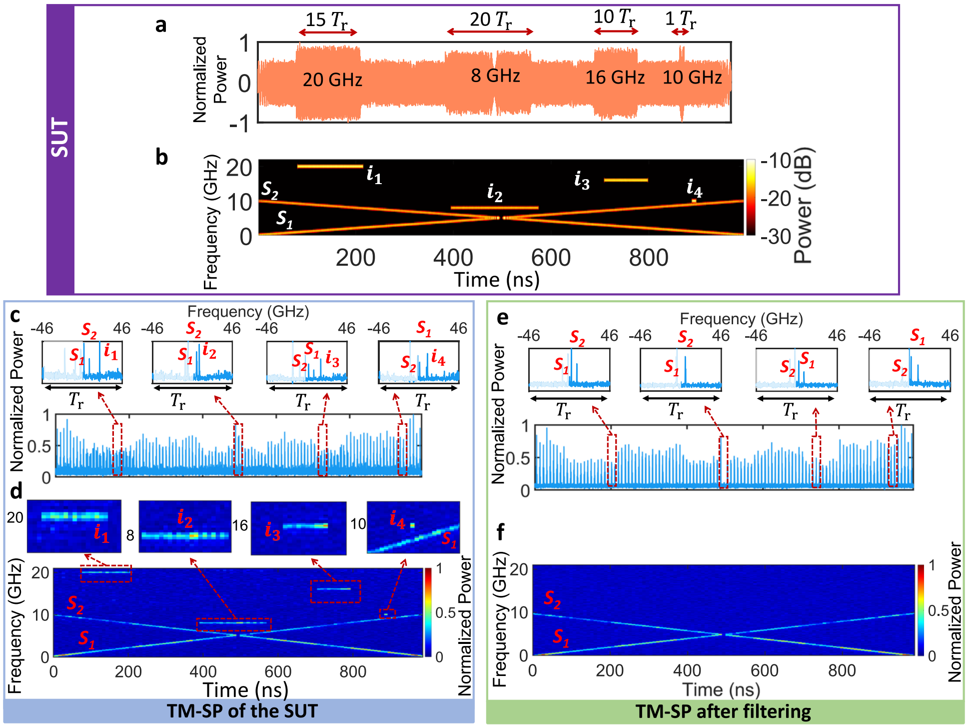

Fig. 3 | Demonstration of highly selective attenuation of nonstationary frequency interferences. a Measured temporal waveform of the SUT, which is composed of two linear-chirped signals (‘S_1’ and ‘S_2’) and several interferences (‘i_1’ – ‘i_4’) with varying frequency locations and temporal durations. **b** Intensity of the numerical STFT, or spectrogram, of the SUT. **c** Measured TM-SP trace at the output of the STFT scheme, with zooms-in around the location of the interferences, each zoomed waveform extending over on analysis period ($T_r \sim 9$ ns). The top axis in each zoomed plot corresponds to the equivalent relative frequency axis. **d** A 2D representation of the measured TM-SP and the close-ups of the interference sections. The different frequency interference components are well discriminated even when extending over a duration as short as the analysis period (9 ns for ‘i_4’). **e** The measured output temporal trace (TM-SP) after the temporal filtering, with the same zoom-in regions as in (**c**), and (**f**), The corresponding 2D representation of the measured TM-SP of the processed signal, confirming that the unwanted interference components are strongly attenuated. SUT: Signal Under Test, STFT: Short-time Fourier Transform, TM-SP: Time-Mapped Spectrogram, 2D: two-dimensional.

every analysis period (T_r) to select the four pulses corresponding to the two chirped signals. Figure 3e, f shows the measured TM-SP trace after the temporal filtering process, as well as the corresponding 2D representation. As expected, the system performs a sufficiently high selectivity to efficiently remove interference i_4 which is spaced by 1 GHz with respect to the double-chirped waveform. A sharper selectivity of 400 MHz has also been experimentally demonstrated (see Fig. 4 in the Supplementary document).

In a final experiment, we showcase the capability of the proposed method to reshape the joint TF distribution of an input stationary broadband wave (Fig. 4). In this case, instead of using simple rectangular pulses for the time-frequency filtering mask, we design more complex filtering masks following arbitrary prescribed patterns. The STFT scheme is now reconfigured to achieve a time resolution (and analysis period) of $T_r \sim 4.5$ ns, corresponding to a frequency resolution of ~220 MHz, and a full analysis bandwidth of $1/t_s \sim 46$ GHz (see “Methods”). The input SUT is a train of sinc-like pulses, periodically spaced by $T_r/3$, purposely designed to exhibit a nearly uniform joint TF energy distribution along its entire duration and full bandwidth (~46 GHz), see Fig. 4a. An arbitrarily prescribed 2D image can then be inscribed along the joint TF energy distribution of the wave within the resolution specifications of the performed TF filtering scheme. In the first example, we successfully re-shape the wave TF distribution into a 2D pattern that resembles an image of the Mona Lisa painting, highlighting the ability to apply different filtering patterns across consecutive windows, see Fig. 4b and “Methods”. The measured TM-SP trace after modulation, Fig. 4c, confirms that the joint TF distribution of the processed wave has a contour proportional to that of the Mona Lisa image, though with the expected degraded resolution mainly due to the down-sampling implemented in the filtering mask generation process, and the limited bandwidth of the 28 GHz scope used for capturing the TM-SP traces. In a second instance, we use the same SUT and design a temporal filtering pattern, Fig. 4d aimed at synthesising a TF distribution following a 2D image of the Chinese character “中”, Fig. 4e. For this purpose, the temporal filtering pattern consists of a sequence of square-like passband pulses with suitable varying widths and centre locations, according to the desired frequency spectrum profile along each of the consecutive analysis periods.

Discussion

We have demonstrated a technique to manipulate in real-time the TF distribution of a wave over broad bandwidths, with high temporal and frequency resolutions and an unprecedented degree of versatility. The proposed concept is demonstrated using off-the-shelf telecommunication components, and it is based on processes and technologies that are widely available in many other frequency regions as well. As such, we anticipate the potential of application of this same concept or similar strategies nearly across the entire EM spectrum. It would be relatively straightforward to utilise the demonstrated fibre-optics scheme for processing ultrafast light waves with frequency bandwidths well beyond those reported here, into the THz regime and above. Towards this aim, we envision the use of nonlinear optics mechanisms, such as cross-phase modulation or four-wave mixing[50–52], in dedicated optical fibres or waveguides for the implementation of the needed temporal phase modulation process at much higher speeds. The proposed concept represents a significant advancement towards manipulation and control of the TF properties of EM waves, and we believe that it will prove particularly useful for the realisation of the cognitive and software-defined paradigms in future wireless and optical communications, intelligent remote sensing

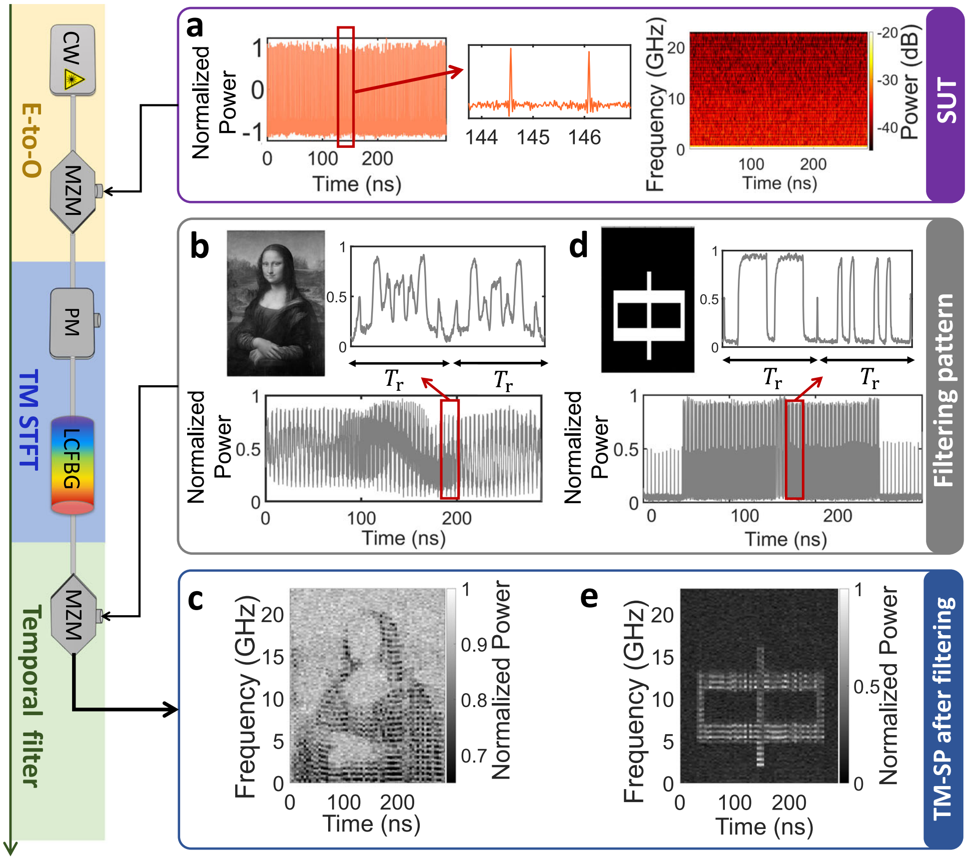

Fig. 4 | Demonstration of user-defined direct synthesis of the wave joint TF distribution. The experimental setup is shown on the left and the results are captured from the real-time oscilloscope. **a** Measured temporal waveform of the SUT, which is composed of periodic sinc-like pulses, forming a nearly uniform spectrogram distribution, over a frequency range up to 23 GHz (positive side) along a duration of ~ 300 ns. The frequency roll-off shown in the numerical STFT shows a good agreement with the measured frequency spectrum of the input pulse train (see Fig. 7 in the Supplementary file). **b** 1D temporal filtering mask mapped from the 2D image of the Mona Lisa painting used to manipulate the TF distribution of the SUT, and a zoom of the user-defined temporal filtering pattern of arbitrary shape. **c** The 2D representation of the TM-SP trace that is measured after the temporal filtering shows that the synthesised spectrogram closely follows the contour of the target image. **d** Using the same SUT as in (**a**), the filtering mask is now designed to craft a joint TF distribution resembling the Chinese character shown at the top left, which is achieved by changing the passband width and centre location of the implemented temporal filtering. The short pulses at the edge of each time window are purposedly introduced to facilitate the synchronisation between the filtering mask and TM-SP. **e** The 2D representation of the TM-SP trace that is measured after the temporal filtering confirms that the synthesised spectrogram closely resembles the target character. The frequency roll-off in the synthesised spectrogram is consistent with that of the input sinc-like pulses (see Fig. 8 in the Supplementary file). SUT: Signal Under Test, STFT: Short-time Fourier Transform, TM-SP: Time-Mapped Spectrogram, 2D: two-dimensional, CW: Continuous-Wave laser, MZM: electro-optic Mach-Zehnder Modulator, PM: electro-optic Phase Modulator, LCFBG: Linearly Chirped Fibre Bragg Grating.

platforms and other systems based on broadband microwave, THz or optical waves.

In the proof-of-concept experiments, the filtering pattern is pre-designed accordingly to manipulate the incoming signal. In this case, the frequency components of the incoming signal need to be precisely known in advance. As such, this approach is ideally suited for applications where the signal characteristics are predetermined, such as in frequency hopping communication systems[22,53] or chirped radar platforms[47]. Moreover, our approach also holds promise for processing unknown incoming waveforms through the generation of the filtering pattern on the fly, either in the digital domain or in an entirely analogue manner.

This work demonstrates advanced versatility based on a photonic method and with low latency, making it well-suited for real-time high-speed signal analysis and processing. Detailed latency estimates provided in the Supplementary (Latency estimation) confirm that the proposed photonic method outperforms DSP engines by orders of magnitude. Nonetheless, it is worth noting that our proposed scheme relies on high-speed electro-optic modulators and electronic AWGs, which may translate into significant cost and power consumption in practical implementations. However, the performance benefits of our proposed system, including high-resolution, real-time TF manipulation over tens of GHz bandwidth, outweigh the added complexity and cost. Equivalent performance specifications achieved through, e.g., DSP approaches, would require channelising a ~ 40 GHz bandwidth signal into smaller few-GHz bandwidth segments[54], as each DSP unit has limited real-time operation bandwidth. In turn, this would translate into a considerable cost and complexity for the resulting overall DSP system. Thus, the low latency advantage and the capability to handle such high-frequency waves in a real-time manner and with notable versatility make our proposed scheme particularly interesting for advanced applications.

Methods

Joint TF manipulation using the short-time Fourier transform (STFT)

The STFT of a signal is generated by applying a windowing function to successive short temporal segments of the signal, then performing a Fourier transform on each segment[15]. Changes in the signal spectrum are then captured over each time slot with a duration determined by the width of each analysed signal segment. This is often referred to as the time resolution of the STFT[15]. Moreover, the uncertainty principle of the Fourier transform implies that the frequency spectrum of each truncated signal segment exhibits a resolution (minimum spacing between two frequency components that are resolved by the Fourier representation) that is of the order of the inverse of the STFT time resolution[15]. As such, for a full manipulation of the TF distribution of a signal, one must be able to modify the signal spectrum with a prescribed minimum frequency resolution, at a speed (i.e., with a refresh rate) of the order of this frequency resolution.

TAI-based time-mapped STFT

The time-mapped STFT process is based on a temporal array illuminator (TAI) phase modulation of the input waveform (SUT), followed by a quadratic spectral phase filtering device[46]. In particular, the temporal phase is composed of a periodic set of multi-level temporal phase shifts that change in groups of q discrete steps, each of time width of t_s, such that the n^{th} phase shift can be expressed as:

$$\varphi_n = -\sigma\pi n^2 \frac{q-1}{q} \tag{1}$$

where $n = 1, 2, \ldots, q$ represents the bin number of each step of the phase modulation profile and $\sigma = \pm 1$. This discrete phase profile then repeats along the time domain, resulting in a periodic phase modulation pattern with a period $T_r = qt_s$. Examples of the temporal phase modulation implemented in the experimental demonstrations reported here are shown in Supplementary Fig. 1. The following spectral phase filtering process can, in practice, be implemented using a second-order dispersive medium, providing a second-order dispersion $\ddot{\phi}$ (defined as the slope of the medium's linear group delay as a function of the radial frequency) that satisfies the following condition:

$$\ddot{\phi} = \sigma \frac{q{t_s}^2}{2\pi} \tag{2}$$

In practice, this spectral phase filtering can be implemented using a simple group-velocity dispersive line (e.g., an appropriate length of single-mode optical fibre). This scheme calculates the Fourier transform (FT) over each consecutive section of duration T_r of the input SUT, in such a way that the resulting consecutive spectra are mapped along the time domain, each extending over a time slot of duration T_r. This mapping is produced according to the following frequency-to-time mapping law

$$\Delta\omega_t \rightarrow \Delta t/\ddot{\phi}, \tag{3}$$

where $\Delta\omega_t$ and Δt are the radial frequency of the input signal and time variable at the system output, both relative to the centre of each analysis window. It can be shown that the maximum frequency extension of the input SUT, or instantaneous analysis bandwidth B of the implemented spectrogram, is just limited by the inverse of the time width t_s of each single-phase step in the modulation profile[46], $B \sim 2\pi/t_s$. This latest condition ensures that the consecutive time-mapped spectra do not interfere with each other. Moreover, the signal frequency bandwidth must be within the spectrogram analysis bandwidth (B). This implies that[46]:

$$\Delta\upsilon_{SUT} \leq \frac{1}{t_s}, \tag{4}$$

where $\Delta\upsilon_{SUT}$ is the full bandwidth of the SUT expressed in natural frequency units. Thus, the full frequency bandwidth of the SUT is ultimately limited by the speed or bandwidth of the phase modulation apparatus in the system.

Through the proposed method, spectral changes in the SUT are captured in every analysis period of T_r. As such, the time resolution of the obtained spectrogram analysis is directly determined by the period length of the phase pattern, T_r (duration of each analysed signal section) and the frequency resolution is inversely related to the time resolution, namely, $\delta\omega_t \sim 2\pi/T_r$. The maximum number of points of the conducted spectral analysis is then defined as $N \sim B/\delta\omega_t$, which is determined by the number of phase steps per period in the phase modulation pattern[25]. As discussed above, at the system output, consecutive time-mapped spectra are spaced by the period $T_r = qt_s$, in such a way that the processing speed (number of FTs calculated per unit of time) is determined by the inverse of this period, namely, $1/T_r = 1/(qt_s)$. A higher processing speed can then be achieved by fixing a shorter period T_r in the design (either by using a shorter t_s or a smaller q factor), but this would unavoidably worsen the achieved frequency resolution. A fine frequency resolution requires a longer analysis window $T_r = qt_s$. The limiting factor for the maximum width of T_r is the required dispersion, as indicated by Eq. 2. For instance, as demonstrated in the results, a 660 MHz frequency resolution was achieved with a dispersion of $\ddot{\phi} \sim 2{,}600\,\mathrm{ps}^2/\mathrm{rad}$ and a finer frequency resolution of 110 MHz required the use of a larger dispersion, i.e., $\ddot{\phi} \sim 15{,}494\,\mathrm{ps}^2/\mathrm{rad}$. Thus, an even finer frequency resolution would require an even larger amount of dispersion. However, a finer frequency resolution would also lead to a larger time resolution and slower tuning speed, as discussed below. On the other hand, the operation bandwidth of the system is related to the time width of each step of the TAI phase profile, $B \sim 2\pi/t_s$ (See supplementary Table 1). This latest specification is mainly limited by the sampling rate of the arbitrary waveform generator that is used to generate the TAI phase. For some of the results presented in this paper, the phase step width is set as a single sampling point of the AWG, i.e., $t_s \sim 1/92$ GHz, fully exploiting the AWG operation bandwidth of 92 GHz. To overcome this bottleneck, a higher-speed AWG, such as a commercially available 256 GS/s AWG[55], could be used to generate a TAI phase with a narrower step width down to $t_s \sim 1/256$ GHz, though this would significantly increase the cost of the system. Note that to accommodate such a TAI phase with a narrower step width, a phase modulator with a larger bandwidth would be also required[56,57].

Design specifications of the performed time-mapped STFT analyses

To analyse the signal in Fig. 2, a temporal phase modulation pattern is designed following Eq. (1) with $q = 139$ phase levels, each with a width of $t_s \sim 10.8$ ps (see Supplementary Fig. 1a). This sets the maximum full analysis bandwidth of the performed spectrogram to $1/t_s \sim 92$ GHz, the analysis period (and time resolution) to $T_r = q \times t_s \sim 1.5$ ns, and the corresponding frequency resolution $\delta\omega \sim 2\pi \times 660$ MHz, allowing for a total of 139 analysis points per spectrum. The phase-modulated light wave is then propagated through a reflective linearly chirped fibre Bragg grating (LCFBG), implementing the required group-velocity dispersion, according to Eq. (2), with a dispersion coefficient $\ddot{\phi} \sim 2{,}600\,\mathrm{ps}^2/\mathrm{rad}$, well over the full bandwidth of the optical modulated SUT. The frequency resolution of the obtained spectrogram can be calculated by estimating the minimum frequency spacing between two adjacent pulses that can be clearly separated, see the zoomed-in region in Fig. 2. The predicted frequency resolution of ~660 MHz would require capturing the TM-SP with a resolution of ~10.8 ps (phase modulation step width). The measured frequency resolution is, however, ~2 GHz rather than 660 MHz, which is mainly limited by the sampling rate of the real-time oscilloscope and the photodiode bandwidth (see Fig. 3 in the Supplementary document). The input and output temporal waveforms shown in Fig. 2 are captured by a high-speed (70 GHz) electrical sampling scope, whereas the TM-SPs are measured using a 28 GHz real-time oscilloscope.

The temporal phase modulation pattern for the results in Fig. 3 is designed with $q = 836$ phase levels, each with a length of $t_s \sim 10.8$ ps and the period length is $T_r = 9$ ns (see Supplementary Fig. 1b), corresponding to a LCFBG with $\ddot{\phi} \sim 15{,}494\ \mathrm{ps}^2/\mathrm{rad}$. To show the reconfigurability of the system, the temporal phase used in Fig. 4 is set as $q = 207$, $t_s = 20.2$ ps with a period of 4.55 ns and with the same LCFBG as that used for the results in Fig. 3. (see Supplementary Fig. 1c). Figure 3a, b shows the measured SUT and its corresponding numerical spectrogram. The frequency of the double-chirped signal (components denoted as S_1 and S_2) ranges from 120 MHz to 10 GHz, and the isolated interferences (denoted as ‘i_m’, with $m = 1, 2, 3, 4$) have durations ranging from $20 \times T_r$ to $1 \times T_r$ and central frequencies ranging from of 8 GHz to 20 GHz. As shown in Fig. 3c, d, the TM-SP enables accurate identification of the individual chirps (i.e., S_1 and S_2) and frequency interferences of the SUT at the expected time and frequency locations.

Temporal filtering mask

To process the time-mapped STFT waveform, the temporal modulation patterns are predesigned according to the frequency-to-time mapping law in Eq. (3). As described, for the results in Figs. 2 and 3, a set of 5 rectangular pulses is used to compose the filtering mask per analysis period of duration T_r. As such, the tuning speed is equal to the time resolution, T_r, which is inversely related to the frequency resolution, as mentioned above. This implies that a faster tuning speed can be achieved by use of a shorter period T_r. In turn, this would result in a higher processing speed, though at the cost of a poorer frequency resolution. In order to precisely manipulate the waveform with a resolution that is limited by the frequency resolution of the TF distribution, a modulation time resolution is needed of the order of the TAI phase modulation step duration t_s. Note that the time width of the modulation pulse can be user-defined and adjusted accordingly. However, insufficient bandwidth of the time-domain filtering pattern (i.e., the use of wider filtering pulses) may result in a deterioration of the filter’s frequency resolution, preventing, for instance, being able to filter out one of the two closely spaced frequencies, while the maximum bandwidth and time resolution of the performed filtering process remain essentially unaffected (see Supplementary − analysis of the impact of the filtering mask bandwidth on system characteristics and Supplementary Fig. 10).

In general, the temporal filtering mask can be mathematically expressed as:

$$h(t) = \sum_p \sum_k \left[a_{pk}\,\mathrm{rect}\left(\frac{t - \frac{T_r}{2} \pm \Delta t_{pk} + pT_r}{\Delta t_{filt}} \right) + \mathrm{rect}\left(\frac{t - \frac{T_r}{2} + pT_r}{\Delta t_{filt}} \right) \right]_{\Delta t_{pk} = \Delta\omega_{pk}/\ddot{\phi}} \tag{5}$$

where t defines the time variable of the temporal pattern, $\mathrm{rect}\left(\frac{t-T}{\Delta t}\right)$ denotes a rectangular function centred at T extending over a total duration of Δt, and pT_r identifies the central time location of each of the analysis periods (with $p = 0, \pm 1, \pm 2, \ldots$).

The first terms in the function in Eq. (5) define the modulation pattern for selecting the desired frequency components, where the parameter Δt_{filt} represents the time width of each of the rectangular pulses, which is chosen to be about t_s in our experiment and Δt_{pk} is obtained from the frequency location $\Delta\omega_{pk}$ (relative to the centre of the corresponding analysis window) of each of the different components (identified by $k = 0,1,2\ldots$) to be selected from the spectrogram distribution in the p^{th} time slot, according to the frequency-to-time mapping law in Eq. (3). The factor a_{pk} defines the relative amount by which the corresponding frequency component is attenuated. The second summation term in the function defined in Eq. (5) corresponds to the location of the DC component (or carrier optical frequency) of the SUT, which needs to be maintained for the realisation of the processed waveform recovery step using the proposed scheme. We recall that this DC term exhibits a significant relative intensity, and as such, it is eliminated in the 2D representation of the measured TM-SP distributions shown here to facilitate observation of the relevant components in the obtained TF distributions. The temporal filtering profile defined by Eq. (5) can be customised by the designer in terms of the number of filtering pulses along every time slot, the basic shape of the pattern, and the time width of each pulse. The relative intensity ratio of the unwanted frequency components with respect to the selected ones is mainly limited by the nominal extinction ratio of the modulation device used for the practical implementation of the time filtering operation.

The filtering pattern in Fig. 4b is directly transferred from the image of the Mona Lisa painting. We first converted the image from RGB to grayscale and employed normalisation of the intensity (i.e., 1 for white and 0 for black). In this case, our goal is to map the target image into the 2D joint TF representation, and we recall that this 2D representation is obtained by vertically plotting the frequency spectrum profile of adjacent temporal analysis windows. As such, the image matrix needs to be resized to have the same number of samples per column as the vertical samples per analysis period in the 2D TF representation, according to the specifications of the performed STFT analysis (i.e., 414 samples in our case); accordingly, the row samples must be fixed to be equal to the total number of analysis periods (64 samples in our case). The temporal filtering pattern can then be obtained by unfolding the 2D matrix into a 1D vector, see Supplementary Fig. 9. In Fig. 4d, we target to carve the 2D TF representation to resemble a Chinese character by precisely filtering the corresponding frequency components at the corresponding time locations. The filtering mask is composed of rectangular pulses of varying width (minimum of t_s) and central locations, designed according to the target Chinese character image. To give an example, as shown in the zoomed-in-region in Fig. 4d, the temporal filtering pattern is designed to select the frequency band from 2 GHz to 16 GHz in the 38th to 40th time slot, corresponding to a passband total time width of $\sim 64 \times t_s$, while in the 12th to 14th and 60th to 62nd time slot, the frequency 5-13 GHz is selected. From the 14th to 60st time slot, the frequency bands 5–7 GHz and 11–13 GHz have been filtered in.

Experimental set-up and specifications of the system

The basic set-up to implement the proposed joint TF filtering approach is shown in Supplementary Fig. 6. The optical carrier for the results in Fig. 2 is generated from a tuneable continuous wave laser (CoBrite-DX) with a central wavelength of 1553.3 nm, and the one for Figs. 3 and 4 is generated from an NKT laser (K80-152-14) centred at 1550 nm. The input microwave SUTs and temporal filtering patterns are all generated from an electronic AWG with a sampling rate of 92 GS/s (Keysight M8196A). An RF amplifier with a bandwidth of 50 GHz (Optilab MD-50) is used to boost the power of the SUT. The input SUT is modulated on the optical carrier through a 40 GHz electro-optic MZM (EOSPACE). To ensure that the optical modulated signal exhibits a nearly flat amplitude over different frequency components, the microwave SUT is properly designed to pre-compensate for the spectral roll-off of the RF amplifier and MZM (see Supplementary Fig. 2).

For the waveform recovery experiments (Figs. 2 and 3), the optical carrier must be kept in the optical modulated SUT. As a result, the MZM is biased to operate over its linear region (~ 4.2 V). Concerning the results in Fig. 4, the input SUT is designed as a periodic set of short pulses, each with a shape defined by the function $sinc[46 \times 10^9 (t \pm T_r/3)]$ to achieve a nearly flat spectrum along the 46 GHz bandwidth. In these experiments, the MZM is biased at 6.1 V to suppress the optical carrier. In all cases, an optical polarisation controller is used before the MZM to optimise the electro-optic modulation process. The optical SUT then enters the TAI-based STFT unit, composed of a 40 GHz electro-optic phase modulator with a half-wave voltage of 3.1 V at 1 GHz (EOSPACE) driven by another channel of the same AWG boosted by a 50 GHz RF amplifier (Optilab MD-50). As described above, the temporal phase pattern is pre-designed according to Eq. (1). An Erbium-Doped Fibre Amplifier (Pritel EDFA) is used before the subsequent dispersive element to compensate for the loss along the system. Concerning the dispersive elements, they are chosen to provide the corresponding amount of group-velocity dispersion, according to Eq. (2), over a sufficiently broad spectral bandwidth (exceeding the optical modulated-SUT bandwidth). For the results presented in Fig. 2, we use an LCFBG providing a total second-order dispersion $\ddot{\phi} \sim 2{,}600\ \mathrm{ps}^2/\mathrm{rad}$, whereas an LCFBG with $\ddot{\phi} \sim 15{,}494\ \mathrm{ps}^2/\mathrm{rad}$ is used for the results of Figs. 3 and 4. Note that other devices can be employed to provide the desired amount of dispersion, such as fibre optic cables. The designed temporal filtering pattern is generated from the third channel of the same AWG followed by a 40 GHz RF amplifier (MD-40) and modulated on the optical pulses after the first LCFBG, using a second MZM with 40 GHz bandwidth and 37 dB extinction ratio (Optilab) following an optical polarisation controller. This MZM is biased at 6.2 V to achieve a high dynamic range. Finally, the microwave TF-filtered waveform is recovered after propagation through a second LCFBG and the O-E conversion using a 50 GHz bandwidth photo-detector (Finisar XPDV2120R). Note that the dispersion of the second LCFBG is the exact opposite of that of the first LCFBG used for the TAI spectrogram. An optical tuneable delay line is placed between the first LCFBG and the second MZM to synchronise the TM-SP trace of the SUT and the temporal filtering mask. The TM-SP trace of the SUTs, the output after temporal filtering, and the microwave SUTs in Figs. 3 and 4 are captured using a 28-GHz bandwidth real-time oscilloscope (Agilent DSO-X 92804 A) without averaging. The real-time oscilloscope is triggered through a reference signal from the electronic AWG with the same length as each incoming microwave SUT. The input microwave SUT and the output recovered processed microwave signal in Fig. 2 are captured using a 70-GHz bandwidth electrical sampling oscilloscope (Tektronix CSA8200), while the time-mapped spectrogram waveforms are obtained from the 28 GHz real-time oscilloscope. Note that the sampling rate of the sampling oscilloscope is set at 2,000 GS/s, and the measured waveform is down-sampled to 92 GS/s to obtain a proper frequency and time resolution in the numerical STFT of the SUT and recovered signal in Fig. 2. Further processing of the captured temporal traces, namely resampling, retiming, and rescaling to the frequency domain, is performed numerically offline. Specifically, each of the measured TM-SP traces is sampled in the real-time scope at a rate of 80 GS/s. This is then resampled to 92 GS/s to ensure uniform results throughout the analysis. The obtained temporal waveform is rescaled to have the frequency information along every analysis period (T_r), according to the corresponding time-mapped frequency factor, aligning the data with the corresponding frequency axis. The resulting 1D vector, now containing the rescaled frequency information along every defined time window, is then reshaped into a 2D matrix. This reshaping allows for the 2D representation of the TF distribution, as depicted in Figs. 2–4. Additional details on the reshaping process are shown in Supplementary Fig. 9.

Data availability

The paper and/or the supplementary information contain all the data needed to evaluate the conclusions. Correspondence and material requests should be addressed to the corresponding author.

References

1. Weiner, A. M. Ultrafast optical pulse shaping: A tutorial review. *Opt. Commun.* **284**, 3669–3692 (2011).
2. Tan, L. & Jiang, J. *Digital Signal Processing: Fundamentals and Applications*. (Academic Press, 2018).
3. Pan, Shilong & Zhang, Y. Microwave photonic radars. *J. Lightwave Technol.* **38**, 5450–5484 (2020).
4. Winzer, P. J. & Essiambre, R.-J. Advanced optical modulation formats. in *Optical Fiber Telecommunications V B (Fifth Edition)* 23–93 (Academic Press, Burlington, 2008).
5. Agrawal, G. P. *Fiber-Optic Communication* Systems. (John Wiley & Sons, 2012).
6. Hui, R. & O'Sullivan, M. *Fiber-Optic Measurement Techniques*. (Academic Press, 2022).
7. Shen, Y., Bootsman, R., Alavi, M. S. & de Vreede, L. C. N. A wideband IQ-mapping direct-digital RF modulator for 5G transmitters. *IEEE J. Solid State Circuits* **57**, 1446–1456 (2022).
8. Wang, C. et al. Integrated lithium niobate electro-optic modulators operating at CMOS-compatible voltages. *Nature* **562**, 101–104 (2018).
9. Oppenheim, A. V., Willsky, A. S. & Nawab, S. H. *Signals & Systems (2nd Ed.)*. (Prentice-Hall, Inc., USA, 1996).
10. Jin, F. & Cao, S. Automotive radar interference mitigation using adaptive noise canceller. *IEEE Trans. Veh. Technol.* **68**, 3747–3754 (2019).
11. Vaezi, M., Ding, Z. & Poor, H. V. *Multiple Access Techniques for 5G Wireless Networks and Beyond*. (Springer International Publishing, Cham, 2019).
12. Ranathive, S., Kumar, K. V., Rashed, A. N. Z., Tabbour, M. S. F. & Sundararajan, T. V. P. Performance signature of optical fiber communications dispersion compensation techniques for the control of dispersion management. *J. Opt. Commun.* **43**, 611–623 (2022).
13. Cameron, R. J., Kudsia, C. M. & Mansour, R. R. *Microwave Filters for Communication Systems: Fundamentals, Design, and Applications*. (John Wiley & Sons, 2018).
14. Capmany, J., Ortega, B. & Pastor, D. A tutorial on microwave photonic filters. *J. Light. Technol.* **24**, 201–229 (2006).
15. Boashash, B. *Time-Frequency Signal Analysis and Processing: A Comprehensive Reference*. (Academic Press, 2015).
16. Al-Yasir, Y. I. A., Ojaroudi Parchin, N., Abd-Alhameed, R. A., Abdulkhaleq, A. M. & Noras, J. M. Recent progress in the design of 4G/5G reconfigurable filters. *Electronics* **8**, 114 (2019).
17. Sun, H., Nallanathan, A., Wang, C.-X. & Chen, Y. Wideband spectrum sensing for cognitive radio networks: a survey. *IEEE Wirel. Commun.* **20**, 74–81 (2013).
18. Ghelfi, P. et al. A fully photonics-based coherent radar system. *Nature* **507**, 341–345 (2014).
19. Shao, H. et al. An investigation of spectral band selection for hyperspectral LiDAR technique. *Electronics* **9**, 148 (2020).
20. Wang, B. & Liu, K. J. R. Advances in cognitive radio networks: A survey. *IEEE J. Sel. Top. Signal Process.* **5**, 5–23 (2011).
21. Miguel et al. Cognitive dynamic optical networks. *J. Opt. Commun. Netw.* **5**, A107–A118 (2013).
22. Liu, Q. & Fok, M. P. Ultrafast and wideband microwave photonic frequency-hopping systems: A review. *Appl. Sci.* **10**, 521 (2020).
23. Serafino, G. et al. Toward a new generation of radar systems based on microwave photonic technologies. *J. Light. Technol.* **37**, 643–650 (2019).
24. Thummaluru, S. R., Ameen, M. & Chaudhary, R. K. Four-port MIMO cognitive radio system for midband 5G applications. *IEEE Trans. Antennas Propag.* **67**, 5634–5645 (2019).
25. Ma, D. & Chen, Y. Time-varying microwave photonic filter for arbitrary waveform signal-to-noise ratio improvement. *Opt. Lett.* **47**, 2186–2189 (2022).
26. Kim, H.-J., Leaird, D. E. & Weiner, A. M. Rapidly tunable dual-comb RF photonic filter for ultrabroadband RF spread spectrum applications. *IEEE Trans. Microw. Theory Tech.* **64**, 3351–3362 (2016).
27. Sun, Y., Wang, S., Chen, J. & Wu, G. Fast and large-range frequency hopping receiving based on simultaneous photonic filtering and digitizing. *Opt. Lett.* **46**, 749–752 (2021).

28. Chan, E. H. W. & Minasian, R. A. High-resolution tunable RF/microwave photonic notch filter with low-noise performance. *J. Light. Technol.* **29**, 3304–3309 (2011).
29. Zhang, W. et al. A system-on-chip microwave photonic processor solves dynamic RF interference in real time with picosecond latency. *Light Sci. Appl.* **13**, 14 (2024).
30. 6G: The Next Horizon. https://www-file.huawei.com/-/media/corp2020/pdf/tech-insights/1/6g-white-paper-en.pdf?la=en.
31. Keysight. N9042B UXA X-Series Signal Analyzer. *Keysight* https://www.keysight.com/ca/en/cmp/2021/n9042b-uxa-x-series-signal-analyzer.html.
32. Khan, F. & Younis, M. I. RF MEMS electrostatically actuated tunable capacitors and their applications: a review. *J. Micromech. Microeng.* **32**, 013002 (2021).
33. Song, K. et al. Compact wide-frequency tunable filter with switchable bandpass and bandstop frequency response. *IEEE Access* **7**, 47503–47508 (2019).
34. Pérez-López, D., López, A., DasMahapatra, P. & Capmany, J. Multipurpose self-configuration of programmable photonic circuits. *Nat. Commun.* **11**, 6359 (2020).
35. Ge, J., Garon, D. A., Liu, Q. & Fok, M. P. Reconfigurable microwave photonic spectral shaper. In *2019 Optical Fiber Communication Conference* (*OFC)* W2A.36 (Optica Publishing Group, 2019).
36. Daulay, O. et al. Programmable integrated microwave photonic filter using a modulation transformer and a double-injection ring resonator. In *2021 European Conference on Optical Communication (ECOC)* 1–4 (2021).
37. Porzi, C., Reza, M., Ghelfi, P., Sorel, M. & Bogoni, A. Silicon-on-insulator microwave photonic filter with widely tunable and reconfigurable flat-top bandpass functionality. *J. Lightwave Technol.* **40**, 6666–6675 (2022).
38. Supradeepa, V. R. et al. Comb-based radiofrequency photonic filters with rapid tunability and high selectivity. *Nat. Photon.* **6**, 186–194 (2012).
39. Ge, J. & Fok, M. P. Ultra high-speed radio frequency switch based on photonics. *Sci. Rep.* **5**, 17263 (2015).
40. Marpaung, D. et al. Low-power, chip-based stimulated Brillouin scattering microwave photonic filter with ultrahigh selectivity. *Optica* **2**, 76–83 (2015).
41. Liu, Y., Choudhary, A., Marpaung, D. & Eggleton, B. J. Gigahertz optical tuning of an on-chip radio frequency photonic delay line. *Optica* **4**, 418 (2017).
42. Han, G., Li, S., Xue, X. & Zheng, X. Photonic time-frequency filter based on the software-defined time-frequency prism. *Opt. Lett.* **47**, 3576–3579 (2022).
43. Konatham, S. R. et al. Real-time gap-free dynamic waveform spectral analysis with nanosecond resolutions through analog signal processing. *Nat. Commun.* **11**, 3309 (2020).
44. Zhu, X., Crockett, B., Rowe, C. M. L. & Azaña, J. Photonics-enabled Nanosecond Scale Real-time Spectral Analysis with 92-GHz Bandwidth and MHz resolution. In *2023 Optical Fiber Communication Conference (OFC)* M1J.5 (Optica Publishing Group, 2023).
45. Crockett, B., Rowe, C. M. L. & Azaña, J. Capturing ultra-broadband complex-fields of arbitrary duration using a real-time spectrogram. *APL Photonics* **8**, 066108 (2023).
46. Azaña, J., Zhu, X., Rowe, C. & Crockett, B. Optical time-mapped spectrograms (II): Fractional talbot designs. *J. Lightwave Technol.* **41**, 5284–5295 (2023).
47. Alland, S., Stark, W., Ali, M. & Hegde, M. Interference in automotive radar systems: Characteristics, mitigation techniques, and current and future research. *IEEE Signal Process. Mag.* **36**, 45–59 (2019).
48. Rameez, M., Pettersson, M. I. & Dahl, M. Interference compression and mitigation for automotive FMCW radar systems. *IEEE Sens. J.* **22**, 19739–19749 (2022).
49. Waldschmidt, C., Hasch, J. & Menzel, W. Automotive radar — from first efforts to future systems. *IEEE J. Microw.* **1**, 135–148 (2021).
50. Li, Z., Xie, Q., Zhang, Y., Zhang, H. & Shu, C. Spectral recovery of broadband waveforms via cross-phase modulation based tunable Talbot amplifier. *Opt. Express* **32**, 17535 (2024).
51. Li, Z. et al. Four-wave mixing based spectral Talbot amplifier for programmable purification of optical frequency combs. *APL Photonics* **9**, 036101 (2024).
52. Fernández, M. P. et al. An ultra-fast temporal talbot array Illuminator. *J. Lightwave Technol.* **41**, 4725–4733 (2023).
53. Li, C., Qi, P., Wang, D. & Li, Z. On the anti-interference tolerance of cognitive frequency hopping communication systems. *IEEE Trans. Reliab.* **69**, 1453–1464 (2020).
54. M, B. H. & Gupta, K. A. Wideband digital channelizer based on spectrum sensing. In *2020 Third International Conference on Advances in Electronics, Computers and Communications (ICAECC)* 1–6 (2020).
55. Keysight. M8100 Series Arbitrary Waveform Generators. *Keysight* https://www.keysight.com/ca/en/products/arbitrary-waveform-generators/m8100-series-arbitrary-waveform-generators.html.
56. Melikyan, A. et al. High-speed plasmonic phase modulators. *Nat. Photon.* **8**, 229–233 (2014).
57. Yu, M. et al. Integrated femtosecond pulse generator on thin-film lithium niobate. *Nature* **612**, 252–258 (2022).

Acknowledgements

This work was supported in part by the Natural Sciences and Engineering Research Council of Canada (NSERC) and the Fonds de recherche du Québec — Nature et technologies (FRQNT). The authors thank Dr. Saikrishna Reddy Konatham for insightful discussions on the proposed time-mapped spectrogram scheme. Benjamin Crockett acknowledges financial support from NSERC through a Postgraduate Scholarship – Doctoral.

Author contributions

X. Z., B. C., and J. A. conceived the idea. X. Z. carried out the theoretical analysis, with inputs from J.A. and B.C. The experimental work was performed by X. Z. and B. C., with assistance from C. M. L. R. and H. S. The reported numerical studies and related data analysis were performed by X. Z., with inputs from B. C., C. M. L. R., and H. S. The manuscript was written by X. Z., H. S., and J. A., with suggestions from all other authors. All authors discussed the results and revised the manuscript. J. A. provided supervision and oversight of the project.

Competing interests

The authors declare no competing interests.

Additional information

Supplementary information The online version contains supplementary material available at https://doi.org/10.1038/s41467-024-53025-7.

Correspondence and requests for materials should be addressed to José. Azaña.

Peer review information *Nature Communications* thanks Emir Salih Magden and the other anonymous reviewer(s) for their contribution to the peer review of this work. A peer review file is available.